



HAL
open science

Waveguide scattering antennas made by direct laser writing in bulk glass for spectrometry applications in the short-wave IR

M. Callejo, M. Bonduelle, A. Morand, G. Zhang, J. Lv, G. Cheng, C. D'amico, R. Stoian, G. Martin

► To cite this version:

M. Callejo, M. Bonduelle, A. Morand, G. Zhang, J. Lv, et al.. Waveguide scattering antennas made by direct laser writing in bulk glass for spectrometry applications in the short-wave IR. *Applied optics*, 2022, 61 (24), pp.7173-7180. 10.1364/AO.464017. ujm-03753503

HAL Id: ujm-03753503

<https://ujm.hal.science/ujm-03753503v1>

Submitted on 13 Oct 2022

HAL is a multi-disciplinary open access archive for the deposit and dissemination of scientific research documents, whether they are published or not. The documents may come from teaching and research institutions in France or abroad, or from public or private research centers.

L'archive ouverte pluridisciplinaire **HAL**, est destinée au dépôt et à la diffusion de documents scientifiques de niveau recherche, publiés ou non, émanant des établissements d'enseignement et de recherche français ou étrangers, des laboratoires publics ou privés.

Waveguide scattering antennas made by direct laser writing in bulk glass for spectrometry applications in the Short-Wave Infrared

M. CALLEJO,¹ M. BONDUELLE,² A. MORAND,^{1,*} G. ZHANG,^{3,4} J. LV,³ G. CHENG,^{3,4} C. D'AMICO,³ R. STOIAN,³ AND G. MARTIN²

¹ Univ. Grenoble Alpes, Univ. Savoie Mont Blanc, CNRS, Grenoble INP, IMEP-LAHC, F-38000, Grenoble, France

² Univ. Grenoble Alpes, CNRS, IPAG, F-38400, Grenoble, France

³ Laboratoire Hubert Curien, UMR 5516 CNRS, Université de Lyon, Université Jean Monnet, 42000 St. Etienne, France

⁴ School of Artificial Intelligence, Optics and Electronics (iOPEN), Northwestern Polytechnical University, 710072 Xi'an, Shaanxi, China

*alain.morand@univ-grenoble-alpes.fr

Abstract: A buried straight waveguide perturbed periodically by 6 antennas composed of sub-micronic cylinder voids is entirely fabricated using ultrafast laser photoinscription. The light scattered from each antenna is oriented vertically and is detected by a Short-Wave Infrared camera bonded to the surface of the glass with no relay optics. The response of each antenna is analyzed using a wavelength tunable laser source and compared to simulated responses verifying the behaviour of the antenna. Those results show the high potential of direct laser writing technique to realize monolithic embedded detectors by combining complex optical functions within a 3D design. A wavelength meter application with a spectral resolution of 150pm is proposed to demonstrate this combination.

© 2022 Optica Publishing Group

1. Introduction

In the recent years, it has been demonstrated that Direct Laser Writing (DLW) using ultrashort laser pulses is a powerful solution to develop integrated photonic devices [1]. DLW provides several advantages compared to the classical planar integrated optic technology. The fabrication process is first a mask-less technique avoiding the use of complex multi-step photo-lithography processes. Secondly, the focusing of an ultrashort laser pulse produces the excitation and a local change of material properties, generating an optical function based on refractive index engineering. The nonlinear absorption, limited to the focal region, gives the possibility to fabricate structures in three dimensions by repositioning the laser spot [2]. By controlling the laser pulse energy and its duration, the glass modification can be tuned from a smooth positive refractive index change (required for the waveguiding structure) to a cavitation-induced negative refractive index change creating submicronic cylinder voids [3–5]. Thus, soft excitation conditions lead to the generation of waveguiding structures until nanoscale scattering centres. This modification in the glass is also ensured by monitoring the shape of the focused light. This allows to have buried waveguides insensitive to surface evolution and to reach symmetric waveguides with a transverse Gaussian profile [6]. The refractive index contrast is rather weak (10^{-3} range), limiting the waveguide bend and the compactness of functions in the component. Nevertheless, the weak numerical aperture reduces the scattering at the output of the waveguide. With the same DLW technology and spatial beam engineering in the shape of non-diffractive Bessel beams, it is also possible to create high aspect ratio void structures with a diameter close to a few hundred nanometers [7]. These elongated void structures made in the vicinity and positioned transverse to the core waveguide

45 can convert a small part of the light going through them into scattered light propagated in the
46 glass wafer. Due to their high refractive index contrast ($\Delta n = n_{silica} - n_{void} = 0.45$ in fused
47 silica), highly efficient scattering centers are made, and they are thin enough to not perturb the
48 propagation of the light mode inside the waveguide. **The use of a small cylinder void diameter is**
49 **also important to ensure a correct sampling of the optical guided wave which must tend ideally to**
50 **a Dirac comb function** . The ability to create both 3D buried waveguides and cylindrical void
51 based scattering centers with the same laser source is a strong advantage of the DLW technology;
52 alternative approaches depend on complex fabrication steps that involve scanning electronic beam
53 or focused ion beam control. Since the 2000s, the association of scattered dots set periodically
54 along a waveguide ending with a mirror has been proposed to sample the stationary waves issued
55 from the superposition of a forward and a backward optical waves. With a sufficient number
56 of sampling centers (typically from one hundred to one thousand), a spectrum can be deduced
57 after a specific Fourier transform as shown in the Stationary Wave Integrated Fourier Transform
58 Spectrometer (SWIFTS) firstly demonstrated in a Gabor configuration [8,9]. Additionally with a
59 low number of sampling centers (from a dozen to twenty), a wavelength meter function can be
60 implemented using an inverted calibration matrix [10]. In a classical approach, the structures are
61 always made associating complex technologies: lift-off and e-beam writing to make submicron
62 metal lines crossing silicon photonic waveguide [9] or integrated glass waveguides [11] or focused
63 ion beam to make slot cavities in lithium-niobate waveguides [12]. In this work, the exploration
64 of DLW is proposed as an alternative to these fabrication methods. The advantages of DLW
65 enable time and cost efficient fabrication of robust wavelength meters. Indeed, the strengths
66 of this technique make it especially attractive as a prototyping tool. In this work, a waveguide
67 and several cylindrical nano-void antennas have been fabricated into a fused silica glass wafer
68 which is then coupled to a Short-Wave Infrared (SWIR) camera to measure the intensity of the
69 signal emitted by each antenna. The control and reproducibility of the response of each antenna
70 measured directly on the camera is a first step before the realization of a SWIFTS by using a
71 higher number of antennas. Despite, the low number of antennas used, another algorithm is used
72 to reach the wavelength meter function proposed previously on niobate substrate [10]. This paper
73 is divided in four sections. Firstly, the integrated optical device is described. Secondly, some
74 results issued from numerical modeling are shown to preview expected results. Thirdly, optical
75 responses obtained with a wavelength tunable laser source are shown and discussed. And finally,
76 the calibration of this same device to work as a wavelength meter is demonstrated.

77 2. Device description

78 The device is composed of a straight waveguide finished by a metallic mirror as shown in figure 1.
79 Light is coupled into the waveguide using the fiber set at the left side. There is a superposition of
80 the forward wave (solid line) and the backward wave (dashed line) inducing a stationary wave
81 inside the waveguide. As the fringe period is λ/n_g , the spatial interference pattern depends on
82 the wavelength and the refractive index of the waveguide n_g . Periodically sampling the stationary
83 wave can give access to the spectral information of the optical light source. Some conditions
84 must nevertheless be respected: firstly, the sampling dot must be much smaller than the stationary
85 wave period, linked to the minimum wavelength of the optical source. Secondly, the proportion
86 of the extracted signal must also be weak enough to leave the stationary wave undisturbed. The
87 efficiency of the scattering center used to convert the evanescent part of the stationary mode
88 into radiated power depends on the refractive index change. It must be high enough to provide
89 sufficient radiated power. Current approaches consist on nano-grooves or thin metallic stripes
90 fabricated on the sample surface. The radiated signal is either imaged on a camera [9, 16] or the
91 pixel array is bonded to the scattering centers to create a compact and optics-free device [11].
92 However, in the SWIR camera, the active area is far from the pixel physical surface (few hundred
93 micrometers), resulting in the need for a specific design of the scattering centers to control the

94 directivity of the radiated light in order to limit crosstalk between sampling dots [12].

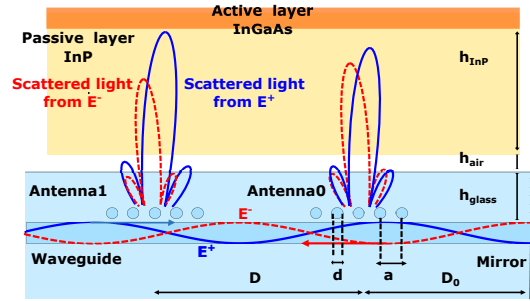


Fig. 1. Principle of the sampling centers radiating the evanescent field of the guided light toward the camera pixel without relay optic. $D = 400\mu\text{m}$ is the distance between two successive antennas and $D_0 = 59\mu\text{m}$ is the distance from the mirror and the first antenna depending of the manual polishing of the input facet. $a = 3\mu\text{m}$ is the period of the cylinder holes in one antenna, transverse to the propagation axis, has a diameter $d < 200\text{nm}$. $h_{\text{glass}} \approx 50\mu\text{m}$ is the reduced glass thickness between the surface and the waveguide position. $h_{\text{InP}} \approx 250\mu\text{m}$ and $h_{\text{air}} = 4\mu\text{m}$. Core waveguide diameter is $50\mu\text{m}$.

95 2.1. DLW features

96 The waveguides were fabricated in fused silica samples using an ultrafast laser photoinscription
 97 technique set in a scan configuration, with a scan of the laser spot perpendicular to the laser
 98 propagation axis. A high repetition rate (100kHz) 180fs laser radiation with an energy per pulse
 99 of $1.5\mu\text{J}$ at 1030nm central wavelength from a Yb:KGW amplified laser system was used in a
 100 moderate focusing configuration ($NA = 0.3$). The irradiation set-up allows to simultaneously
 101 control the time and space envelope of the laser pulse by changing its spectral and spatial
 102 phase. In a fused silica wafer, where bulk refractive index is $n_g = 1.444$ at $\lambda = 1.55\mu\text{m}$, the
 103 refractive index modification obtained is in the range of $10^{-3} - 10^{-4}$. Due to the small refractive
 104 index modification, mode field diameter is large allowing to easily set a scattering center in the
 105 evanescent part without degrading the waveguide core. This technique allowing to obtain large
 106 circular cross-section waveguide photo-inscription modes is based on the method reported "beam
 107 slit-shaping" [17, 18]. In a second step, in order to generate the dielectric discontinuity useful
 108 for the scattering center, a non-diffractive irradiation procedure is used to generate a series of
 109 one-dimensional voids, transverse to the propagation axis at $3\mu\text{m}$ from the waveguide core edge,
 110 with a characteristic section below 200nm and an axial dimension above of $150\mu\text{m}$. **Diameter**
 111 **of 50nm has been already realized but a section of 200nm is a good compromise between**
 112 **reproducibility and the length part sampled**. The same ultrafast Yb:KGW amplified system at a
 113 repetition rate of 100kHz, a duration of 2ps and an energy per pulse of $50\mu\text{J}$, is used. Instead of
 114 more common Gaussian laser beams prone to nonlinear distortion effects, picoseconds pulse
 115 Bessel beams with 10° half-cone angle (inside the material) were employed to generate enough
 116 energy concentration to trigger material cavitation. The technique allows to avoid diffraction
 117 and non linear distortions in order to create axially uniform localized uni-dimensional excitation
 118 domains inside the material. Five Bessel voids arranged at a period close to $a = 3\mu\text{m}$ constitute
 119 an antenna. All these voids form a small grating to scatter light in specific directions. Ideally,
 120 the period should be $a = \lambda/n_{\text{eff}}$ to allow a scattering direction close to the vertical axis but
 121 this value is hard to obtain experimentally at the present wavelength ($1.55\mu\text{m}$) due to technical
 122 limitations. To avoid the positioning complexity when stitching the voids in a close packing, a
 123 higher order of the grating has been chosen, approximately three times higher. The consequence

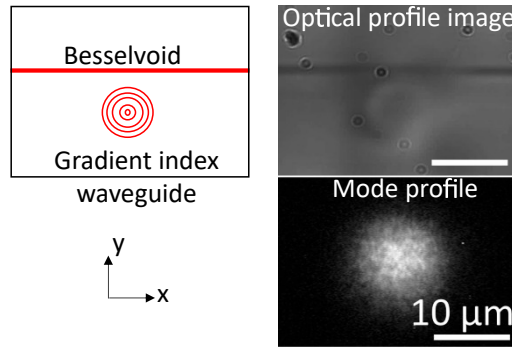


Fig. 2. Waveguide profile schematic on the surface (x, y). Optical image of the profile waveguide on the same surface with the elongated Bessel void photo-written transverse to the propagation axis (z) at $3\mu\text{m}$ from the waveguide core edge.

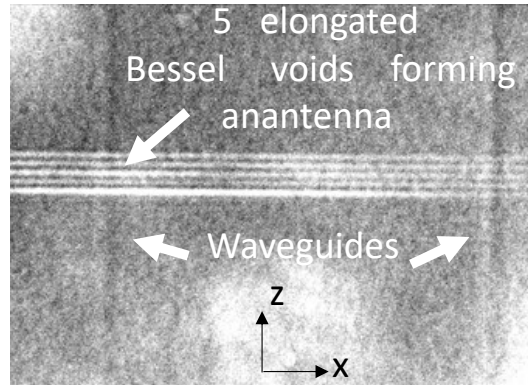


Fig. 3. Image of an antenna composed of 5 elongated Bessel voids over two photo-inscribed waveguides on the surface (xz).

124 is the apparition of a few Bragg orders while sampling the radiated diagram of one antenna. In
 125 figure 2, a transverse section image of the waveguide associated to elongated Bessel voids is
 126 firstly shown. With the same scale, the intensity repartition of the mode observed in the second
 127 figure is larger than the core waveguide. In figure 3, an image of one antenna realized above two
 128 waveguides is shown too. Each elongated Bessel void is made above few waveguides allowing to
 129 test different straight waveguides.

130 The distance $D = 400\mu\text{m}$ is then set to avoid overlapping between each antenna on the detector.
 131 After the writing process, different polishing steps are done. Firstly, a polished procedure is
 132 applied at the input and output facets to access to the waveguide. Indeed, due to scattering effects
 133 perturbing the DLW process, the end and the beginning of the waveguide are made at $400\mu\text{m}$
 134 from the initial facet. Secondly, the top surface is polished to reduce the glass thickness between
 135 the surface and the waveguide position from $400\mu\text{m}$ to approximately $50\mu\text{m}$. It is done to avoid
 136 too much angular diffusion of the extracted beam before reaching the detector in order to reduce
 137 the crosstalk.

138 2.2. Set-up

139 The near infrared sensor used (G12242-0707W) is provided by Hamamatsu without the glass
 140 window. It is a 2D InGaAs camera with a resolution of 16384 (128×128) pixels and a pitch of

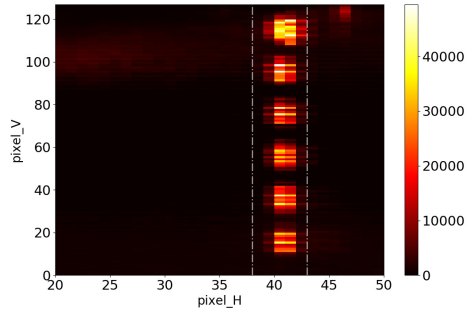


Fig. 4. Image issued from the camera at the wave number $\sigma = 6250.0\text{cm}^{-1}$ ($\lambda = 1.6\mu\text{m}$). The mirror is set at the vertical top part. The antenna 0 close to the $\text{pixel}_V = 110$ is the antenna set closer to the mirror. The intensity zones are associated to the scattering of each antenna. In the vertical direction, the scattering zone is enlarged due to the Bragg orders issued from the void cylinder grating. In the horizontal direction, the enlargement is smaller only associated to the waveguide mode width higher than $10\mu\text{m}$.

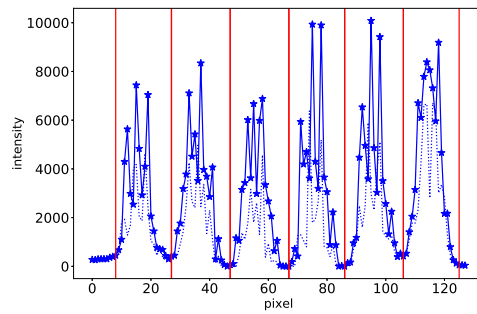


Fig. 5. Integration of the signal along the horizontal axis over few pixels. The vertical lines correspond to area boundaries of each antenna. The power of each antenna is calculated from the intensity integration over each segment. Line with marker \star : $\sigma = 6250.0\text{cm}^{-1}$ ($\lambda = 1.6\mu\text{m}$). Dashed line: $\sigma = 6622.5\text{cm}^{-1}$ ($\lambda = 1.51\mu\text{m}$).

141 $20\mu\text{m}$ in a TO-8 package. An anti-reflection layer is set at the surface of the InP layer of the
 142 sensor whose thickness is approximately $250\mu\text{m}$. All the electrical bondings and electric circuits
 143 are under the surface detector, allowing to approach the glass wafer very close to the pixels.
 144 Different micro-positioners (3D axis and rotation axis) are used to set the detector above the glass
 145 chip that is kept still by a vacuum contact. Another 3D micropositioner is used to control the
 146 fiber injection. Finally the major electric field of the polarization-maintaining fiber is oriented
 147 parallel to the void cylinders. To calibrate the device, a polarized wavelength tunable laser source
 148 is used. To scan the response of the device following the wavelength, the source's trigger output
 149 is used and connected to the trigger input of the detector. So, at each front edge of the trigger
 150 clock corresponding to a wavelength change, an image acquisition is recorded. In figure 4 and 5,
 151 an example of an image is shown. The waveguide is initially aligned to one of the sensor axis.
 152 6 groups are clearly observed corresponding to the 6 antennas. The vertical direction is the
 153 propagation axis of the waveguide. The radiation power spreading in the transverse axis over
 154 few pixels can be observed. The 2D image is then converted in a 1D trace integrating the power
 155 detected along the transverse axis. 3 to 4 peaks are detected in each antenna group corresponding
 156 to different Bragg orders.

157 3. Modeling results

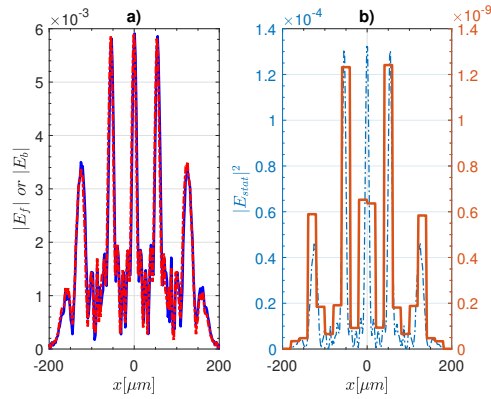


Fig. 6. a) Superposition of the forward field modulus $|E_b|$ (full line) and the backward field modulus $|E_f|$ (dashed line) of the scattering field at the detector position. b) Superposition of the stationary intensity (Dashed line) and the same intensity detected integrated on the pixels (Full line). $\lambda = 1544\text{nm}$ or $\sigma = 6477\text{cm}^{-1}$ with a length of $100\mu\text{m}$ between the antenna and the mirror and an hole period $a = 3.22\mu\text{m}$.

158 The field emitted by a single antenna is simulated with a specific home-made numerical tool.
 159 The method based on a Fourier modal decomposition is already described in [12] where it is
 160 applied to a Lithium Niobate waveguide. For the simulation, the DLW waveguide is replaced
 161 by a step-index waveguide: a core waveguide with a thickness of $2\mu\text{m}$ and a refractive index of
 162 1.446 surrounded by a refractive index of 1.444. The glass thickness between the glass wafer
 163 surface and the core waveguide is $50\mu\text{m}$. Since the image sensor is not in direct contact with the
 164 glass surface, a $4\mu\text{m}$ air gap is included between the glass and the InP layer. The thickness of the
 165 passive InP layer before the camera active layer is equal to $250\mu\text{m}$. The shape of the holes is
 166 approximated by a square ($100\text{nm} \times 100\text{nm}$) filled with air. Due to the size of the multilayer, 801
 167 harmonics are chosen in the fully vectorial tool used in the first step to ensure the convergence.
 168 A length of $100\mu\text{m}$ is set between the mirror and the antenna center. This distance has been
 169 chosen in order to be able to properly sample the stationary wave intensity in a wavelength range

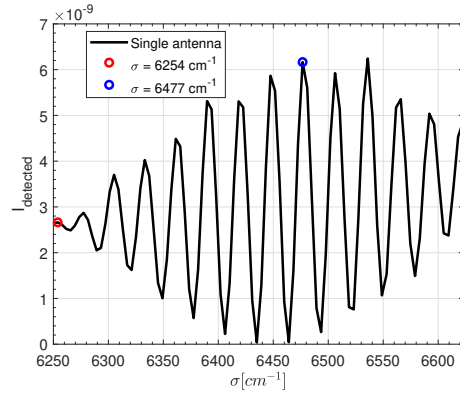


Fig. 7. Evolution of the intensity of one antenna as a function of σ with a length of $100\mu\text{m}$ between the antenna and the mirror and an hole period $a = 3.22\mu\text{m}$. Optimal case with one fringe packet or one lobe of the envelope.

170 from 1510nm to 1600nm or a wave number from 6250cm^{-1} to 6623cm^{-1} . Finally, the mirror is
 171 considered perfect with an amplitude reflection $r = -1$. The modelization of the far radiated
 172 field in the active zone of the detector is made in two steps. First of all, the radiation pattern in
 173 the first micrometers of the InP layer is numerically modeled with a 2D Aperiodic Fourier Modal
 174 Method (AFMM) in guided configuration [13]. The electromagnetic (EM) fields were calculated
 175 along a line parallel to the waveguide propagation axis in the InP layer $0.5\mu\text{m}$ above the interface
 176 InP layer. Secondly, the radiation pattern of the light diffracted in each antenna was extrapolated
 177 into the far field with the Helmholtz - Kirchhoff diffraction theory [14, 15] in which the Green
 178 function is approximated by an exponential one instead of Hankel functions. An antenna of 5
 179 voids with a period of $3\lambda/n_g = 3.22\mu\text{m}$ is firstly simulated corresponding to the ideal case (hole
 180 period exactly matching a multiple of λ/n_g). In figure 6, different scattered field moduli are
 181 shown in the detector area. In this optimized case, the forward and backward field modulus (on
 182 the left figure) are well superposed ensuring a high contrast of the stationary wave intensity (on
 183 the right figure). In this last figure, the intensity evolution detected by each pixel (full line) is
 184 also shown. The scattered light is composed of 5 Bragg orders. The width of each Bragg peak is
 185 proportional to the number of voxels in a single antenna and its shape can be approximated by
 186 a sinus cardinal function, whereas the envelope evolution is linked to the average shape of the
 187 voxel chosen. The positions of the peaks are dependent on the wavelength. If the wave number
 188 is decreased, the forward scattered field is not symmetric any more, reducing its overlapping
 189 with the backward scattered field. The contrast issued from the intensity calculation in this case
 190 decreases as shown in figure 7. A worse case can be reached when the wave number is close to
 191 $\sigma = 6250\text{cm}^{-1}$ where a zero of the forward scattered field is superposed to a maximum of the
 192 backward scattered field. For smaller wave number, a new fringe packet can appear but with a
 193 smaller envelope contrast. Indeed, this effect can be observed when voxel period a is reduced:
 194 the results for $a = 3\mu\text{m}$ are shown in figure 8 and figure 9. The Bragg order maxima are clearly
 195 separated. Nevertheless, an overlapping is always possible but the forward and backward field
 196 amplitudes are highly different. The principal sinus cardinal lobe of the forward field is located
 197 on the secondary lobe of the backward field with a smaller amplitude. Each previous peak of the
 198 intensity evolution are separated in two peaks (one from the forward wave and the other from the
 199 backward wave). A fringe packet can be observed but the contrast maximum calculated at 90%
 200 in the optimized case falls at 20% in this case. As the period achieved with the DLW method is
 201 closer to $a = 3\mu\text{m}$ rather than $a = 3.22\mu\text{m}$, all the contrast results shown in the next part are
 202 affected by the non-optimized hole period.

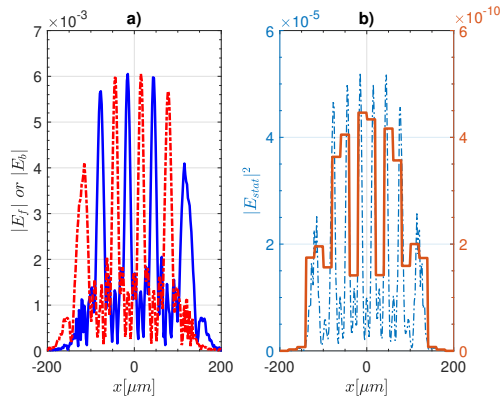


Fig. 8. a) Superposition of the forward field modulus $|E_b|$ (full line) and the backward field modulus $|E_f|$ (dashed line) of the scattering field at the detector position. b) Superposition of the stationary intensity (Dashed line) and the same intensity detected integrated on the pixels (Full line). $\lambda = 1579\text{nm}$ or $\sigma = 6333\text{cm}^{-1}$ with a length of $100\mu\text{m}$ between the antenna and the mirror and an hole period $a = 3\mu\text{m}$.

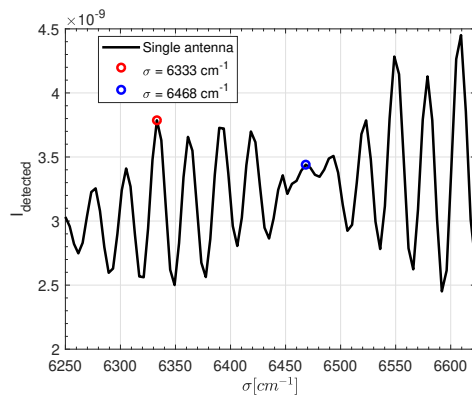


Fig. 9. Evolution of the intensity of one antenna as a function of σ with a length of $100\mu\text{m}$ between the antenna and the mirror and a hole period $a = 3\mu\text{m}$. Sub optimal case with two fringe packet or a zero between the lobes of the envelope.

4. Antenna response measure versus wave number

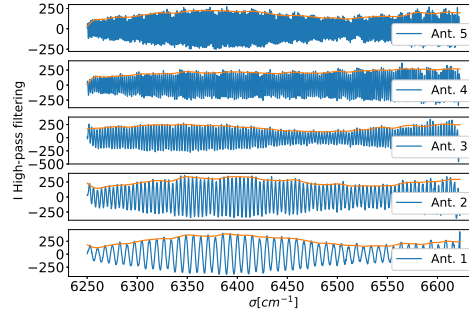


Fig. 10. Intensity response of each antenna after pixel integration as a function of the wave number (except the antenna 0 which is disturbed by the mirror reflection). The modulated evolution has been previously filtered by a Butterworth band-pass filter, and the envelope signal is issued from the Hilbert transform followed once again by a Butterworth low-pass filter.

204 To obtain the power emitted by each antenna, the profile shown in figure 5 must be split in 6
 205 segments of width $D = 400\mu\text{m}$ defined by the successive vertical lines. The power in each zone
 206 is then integrated to define the radiated power $P_i(\sigma)$ emitted by the antenna i . Using a tunable
 207 source, the wavelength is swept from 1510nm to 1600nm with a step of 10pm. The evolution
 208 of the $P_i(\sigma)$ signal is a combination of a periodical oscillation (the interference signal) with
 209 an amplitude envelope and a wavelength dependent offset (mean value of the oscillation). The
 210 analysis of this signal can be used to obtain useful insight into the properties of the scattering
 211 centers fabricated using the DLW technique. The first step for the analysis of the signal is to
 212 separate the mean value from the interference signal. This is achieved by means of a Butterworth
 213 band-pass filter applied twice (equivalent to a filter of order 8 and zero delay) to avoid ripples in
 214 the bandwidth zone. This treatment is coded in Python using the function `butter` issued from the
 215 library `scipy.signal`. With a wavelength step of $\Delta\lambda = 20\text{pm}$ (or $\Delta\sigma = 0.083\text{cm}^{-1}$),
 216 the low and high cut-off frequencies used as inputs are respectively $0.05/f_{\text{max}}$ and $2/f_{\text{max}}$ with
 217 $f_{\text{max}} = 1/(2\Delta\sigma)$. The result of the filtering is shown in figure 10. The oscillation period of
 218 each antenna is directly related to the distance between the antenna and the mirror: the period
 219 decreases as the distance to the mirror increases. The envelope can be extracted by means of a
 220 Hilbert transform followed by a low-pass filter to remove ripples from the result. The envelope of
 221 the oscillation is shown in figure 11.

222 The envelope evolution shape depends on the number of void cylinders used in a single antenna.
 223 As the hole period is close to $a = 3\mu\text{m}$, the overlapping between the forward and backward
 224 scattered fields before the intensity conversion is not optimized, reducing the contrast of the fringe
 225 packet observed as shown in the modelization section in figure 9. The optimized fringe packet
 226 is expected to be centered at the wave number 6925cm^{-1} , outside of the wave number range
 227 observed. In theory, a zero contrast is expected between two successive fringe packets. This
 228 zero appears if all voids are identical (same shape and same size). If they are not, the scattering
 229 of one Bragg order is modified and the narrow peak evolution is not a sinus cardinal function
 230 anymore. This result can induce an overlapping change between the forward and backward fields.
 231 Having different hole sizes in a single antenna can be seen as an apodization of the fringe packet,
 232 leading to the removal of the zero contrast. A simulation has been made choosing 5 holes with
 233 the following arbitrary widths of 100, 140, 120, 200 and 180nm instead of the single width of
 234 100nm used in the modelization part. The intensity evolution of an antenna following the wave

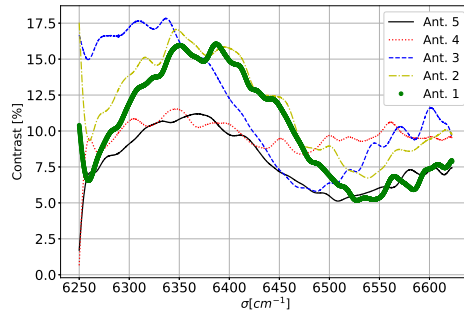


Fig. 11. Evolution of the contrast issued from the previous envelopes as a function of the wave number. The number in the legend is associated to the antenna i studied.

235 number is given in figure 12 for a period $a = 3\mu\text{m}$. The contrast evolution calculated becomes
 236 smoother than the single hole width case and always remains far from 0. It is clearly a hole width
 237 dispersion which can explain the contrast evolution measured.

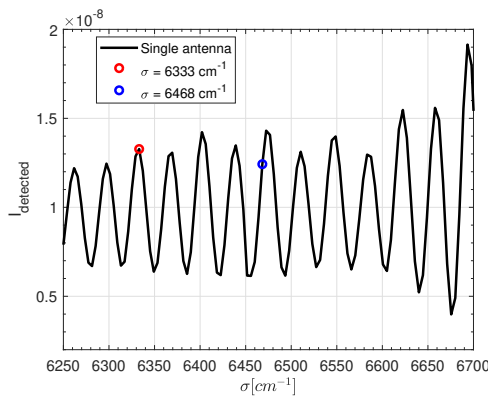


Fig. 12. Intensity evolution as a function of σ simulated for one antenna with a length of $100\mu\text{m}$ between the antenna and the mirror, and an hole period $a = 3\mu\text{m}$. Effect of manufacturing non uniform holes: 5 holes with the following widths 100, 140, 120, 200 and 180nm instead of having uniform holes with a width of 100nm. The envelope amplitude no longer goes to zero between two successive fringe packets or lobes.

238 A maximum contrast of 17.5% is obtained from the measurement of the device. This contrast
 239 is slightly smaller than the predicted value of 19% for the case of identical holes of width 100nm.
 240 This maximum contrast changes from one antenna to another. It depends on the fabrication
 241 accuracy but also on the differential loss between both the forward and backward waves. Indeed,
 242 the interference is maximized when the two waves have the same amplitude. However, due to the
 243 different path followed and the signal extracted by the neighboring antennas, this configuration
 244 changes from one antenna to another.

245 Nevertheless, the minimum contrast position should be the same for each antenna if dispersive
 246 effects in the waveguide are neglected. As shown in figure 9 and figure 7, this position depends on
 247 the voxel period of the antenna and can be used to analyze the reproducibility of the void cylinder
 248 period in each antenna. A wave number shift can be observed, which is analysed in figure 13. The
 249 diamond corresponds to simulated minimum position using the previously mentioned numerical

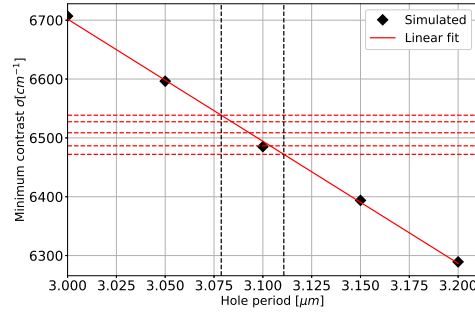


Fig. 13. Evolution of the simulated minimum contrast position as a function of the period of the cylinder holes. The horizontal lines correspond to the measured values issued from the 5 previous antennas characterized. The vertical lines are respectively an estimation of the minimum period and of the maximum period of the antennas realized.

250 tool [12]. The horizontal lines added on the figure are the minimum contrast wave number
 251 issued from the previous measurements of the 5 characterized antennas. The period a of the void
 252 cylinder is estimated between $3.078\mu\text{m}$ and $3.111\mu\text{m}$. The accuracy of this period is $\pm 35\text{nm}$.
 253 This evolution can also appear in a single antenna.

254 5. Fast Fourier transform of the previous signals

255 From the intensity evolution as a function of the wave number, the position of each antenna can
 256 be obtained using a Fast Fourier transform. A Welch [19] method has been chosen in association
 257 with a Bartlett-Hann window and a padding method (4 more sampling elements). **The Welch's**
 258 **method computes an estimate of the power spectral density by dividing the data into overlapping**
 259 **segments, computing a modified periodogram for each segment and averaging the periodograms.**
 260 **And to limit the ripples in the frequency domain after a Fourier transform due to a rectangular**
 261 **window, a triangular window is used for tapering the signal.** The noise is reduced at the expense
 262 of the resolution. The spectrum for each antenna is normalized by its maximum value and shown
 263 in figure 14. Each graph on the figure is the superposition of each single antenna's spectrum.
 264 The peak position gives the spatial position of the antenna. Crosstalk appears if the signal of
 265 one antenna shows at the position of another antenna. Spectra of the 5 antennas for different
 266 laser polarizations are shown. The separation D between each antenna associated to the single
 267 antenna scattering allows to obtain a low crosstalk between each antenna in the TE polarization
 268 case. Changing the polarization state, the crosstalk increases with the apparition of peaks with
 269 non-negligible amplitudes at wrong positions. This is due to the radiated diagram of the TM
 270 case cancelling the vertical propagation direction. The highest crosstalk is observed on the last
 271 two antennas. However this effect remains reasonable in our case. It is worth noting that the
 272 separation between the antennas is enough to record a major part of the TM radiated diagram.
 273 For smaller separation, the device will be more sensitive to the polarization. Each peak is then
 274 close to a Gaussian shape which can be used to fit each of them. In this way, the antenna position
 275 can be determined with an accuracy close to a few micrometers as shown in Table 1. From a
 276 linear fit of the antenna position versus the antenna number, it is notably interesting to determine
 277 the distance D_0 between the first antenna and the mirror as well as the spatial separation D
 278 between two successive antennas. Indeed, the value of D_0 is difficult to determine precisely after
 279 the polishing steps. The respective values calculated from the fitting are $D = 402 \pm 1\mu\text{m}$ and
 280 $D_0 = 59 \pm 2\mu\text{m}$.

281 **6. Wavelength meter**

282 Spectral information can be extracted from our system with a reduced number of antennas.
 283 Therefore, all the pixels analysed along a propagation axis line are used to define a calibration
 284 matrix with a first wavelength scan from 1510nm to 1600nm and a step of 40pm. This calibration
 285 gives a matrix with a shape $N_{Pixel} \times N_{\lambda}$ with $N_{Pixel} = 128$ the pixel number along a line and
 286 $N_{\lambda} = 1751$ the number of scanned wavelengths. The intensity pixel vector I_p measured can then
 287 be linked to the wavelength vector to find λ as $I_p = M\lambda$. Two methods are then proposed. The
 288 first one is a least mean square solution to minimize the norm $|I_p - M\lambda|^2$. The second solution
 289 consists in directly calculating $M_f^{-1}I_p$ and select the maximum value. M_f is not the inverted
 290 matrix of M but the pseudo inverse matrix where all values smaller than $r_{cond} \cdot \max(SVD)$ are
 291 forced to zero with $1 \geq r_{cond} \geq 0$ and SVD a vector containing the singular values of M . The
 292 value of the cutoff has been manually chosen to be $r_{cond} = 0.4$.

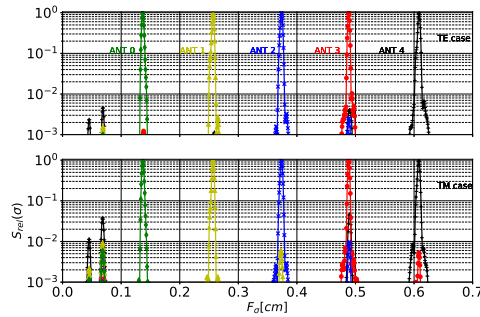


Fig. 14. Spectrum of the intensity evolution for different polarization states. $S_{rel}(x) = \sum S_{rel,i}(x)$ and $S_{rel,i}(x)$ is the power issued from the antenna i and normalized as $S_{rel,i}(x) = P_{Ant,i}(x) / \max(P_{Ant,i}(x))$. From the up, the first and the second graphs are respectively for the TE polarization (0°) and TM polarization (90°) cases. Each peak is associated to the response of a single antenna studied.

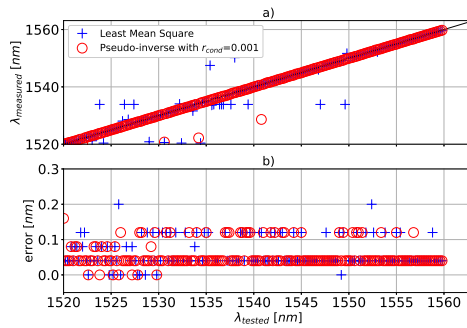


Fig. 15. a) Comparison of the two methods used to analyse the wavelength meter efficiency (Least mean square method and Pseudo inverse matrix method with $r_{cond} = 0.001$). b) Evolution of the error between the reference and the wavelength tested.

293 The effectiveness of these methods has been tested by using another wavelength sweep
 294 measurement, performed under the same conditions but with a different wavelength step of
 295 200pm, from 1520nm to 1560nm. The results of both methods are shown in figure 15. Some

296 cases are not well restored by both methods, and in particular for the least squares approach (+
 297 markers). There are more + markers than o markers. But the pseudo inverse method seems to
 298 be more efficient notably for wavelengths higher than 1540nm. It is noteworthy that the error
 299 is under 0.15nm in the wavelength range observed despite the limited number of antennas. To
 300 improve this method with the same antenna number, it would be more interesting to use antennas
 301 with different period, size ... This is a first step to analyse and confirm the response of this
 302 radiated power extraction solution to sample the stationary wave of an integrated waveguide.

n	1	2	3	4	5	Error
$f/2n_g$ [μm]	467	872	1277	1686	2091	± 10

Table 1. Evolution of the spatial peak position issued from the intensity evolution spectrum.

303 Conclusion

304 A novel approach to signal sampling using DLW voxels and waveguides has been proposed. It is
 305 demonstrated that each scattering center, made by a group of parallel and periodic elongated
 306 Bessel nano-voids (an antenna), is able to transversally scatter a signal which is proportional to
 307 the integrated optic stationary wave inside the waveguide at a given discrete position from the
 308 end mirror. The measured spectral response is close to the expected response. The wavelength
 309 scan can be used to give information about the morphology of the Bessel nano-voids. The
 310 reproducibility of the DLW technology is from our point of view sufficient to test it along a longer
 311 waveguide with a higher number of antennas in order to implement a SWIFTS. However, in order
 312 to increase the contrast and have a more compact device, the period of the nano-voids forming an
 313 antenna must be chosen closer to $p\lambda/n_{eff}$ with p an integer. In this paper, the achieved period is
 314 close to $a = 3.1\mu\text{m}$ nm rather than $a = 3.22\mu\text{m}$, thus inducing a change of Bragg orders and
 315 limiting the contrast to 17.5% instead of an expected value close to 90% in the optimized case.
 316 For future improvements the challenge will be the reduction of this period to $p = 1$, In this case,
 317 only one Bragg order will be excited by an antenna ensuring high contrast, large wavelength
 318 bandwidth to analyse and reduced cross-talk.

319 **Funding.** The authors acknowledge funding from ASHRA (Action Specifique Haute Resolution Angulaire)
 320 from INSU-CNRS, LabEx FOCUS ANR-11-LABX-0013 and LabEx Manutech-SISE ANR-10-LABX-0075.
 321 G. Zhang acknowledges China Scholarship Council fellowship.

322 **Disclosures.** The authors declare no conflicts of interest.

323 References

- 324 1. K. M. Davis, K. Miura, N. Sugimoto and K. Hirao "Writing waveguides in glass with a femtosecond laser," Opt. Lett.
 325 **21**, 1729–1731 (1996).
- 326 2. A. Rodenas, G. Martin, B. Arezki, N. Psaila, G. Jose, A. Jha, L. Labadie, P. Kern, A. Ajoy and R. Thomson
 327 "Microstructuring of Nd: YAG crystals by proton-beam writing," Opt. Lett. **37** 392–394 (2012).
- 328 3. M. K. Bhuyan, F. Courvoisier, P. Á. Lacourt, M. Jacquot, R. Salut, L. Furfaro and J. M. Dudley "High aspect ratio
 329 nanochannel machining using single shot femtosecond Bessel beams," Appl. Phys. Lett. **97** 081102 (2010).
- 330 4. M. Bhuyan, P. K. Velpula, J. P. Colombier, T. Olivier, N. Faure and R. Stoian "Single-shot high aspect ratio bulk
 331 nanostructuring of fused silica using chirp-controlled ultrafast laser Bessel beams," Appl. Phys. Lett. **104** 021107
 332 (2014).
- 333 5. R. Stoian, M. Bhuyan, G. Cheng, G. Zhang, R. Meyer, and F. Courvoisier "Ultrafast Bessel beams: advanced tools
 334 for laser materials processing," Adv. Opt. Technol. **7** 165–174 (2018).
- 335 6. C. D'Amico, G. Cheng, C. Maclair, J. Troles, L. Calvez, V. Nazabal, C. Caillaud, G. Martin, B. Arezki, E. LeCoarer,
 336 P. Kern and R. Stoian "Large-mode-area infrared guiding in ultrafast laser written waveguides in Sulfur-based
 337 chalcogenide glasses," Opt. Express **22** 13091–13101 (2014).

- 338 7. Zhang Z., Cheng G., Bhuyan M., D'Amico C. and Stoian R. "Efficient point-by-point Bragg gratings fabricated in
339 embedded laser-written silica waveguides using ultrafast Bessel beams," *Opt. Lett.* **43** 2161–2164 (2018).
- 340 8. Thomas F., Heidmann S., De Mengin M., Courjal N., Ulliac G., Morand A., Benech P., Le Coarer E. Martin G.
341 "First results in near and mid IR lithium niobate-based integrated optics interferometer based on SWIFTS-Lippmann
342 concept," *J. Light. Technol.*, **32** 3736–3742 (2014).
- 343 9. Le Coarer E., Blaize S., Benech P., Stefanon I., Morand A., Lerondel G., Leblond G., Kern P., Fedeli J-M and Royer
344 P. "Wavelength-scale stationary-wave integrated Fourier-transform spectrometry," *Nat. Photonics* **1** 473–478 (2004).
- 345 10. Bonduelle M., Heras I., Morand A., Ulliac G., Salut R., Courjal N. and Martin G. "Near IR stationary wave Fourier
346 transform lambda meter in lithium niobate: multiplexing and improving optical sampling using spatially shifted
347 nanogroove antenna," *Appl. Opt.* **19** D83–92 (2021).
- 348 11. Bonneville C., Thomas F., De Mengin Poirier M., Le Coarer E., Benech P., Gonthiez T., Morand A., Coutant
349 O., Morino E., Puget R. and Martin B. "SWIFTS: a groundbreaking integrated technology for high-performance
350 spectroscopy and optical sensors," *Proceeding SPIE MOEMS Miniaturized Syst. XII* **86160M** (2013).
- 351 12. Morand A., Heras I., Ulliac G., Le Coarer E., Benech P., Courjal N and Martin G. "Improving the vertical radiation
352 pattern issued from multiple nano-groove scattering centers acting as an antenna for future integrated optics Fourier
353 transform spectrometers in the near IR," *Opt. Lett.* **44** 542–545 (2019).
- 354 13. Bucci D., Martin B. and Morand A. "Application of the three-dimensional aperiodic Fourier modal method using arc
355 elements in curvilinear coordinates," *J. Opt. Soc. Am. A* **29** 367–373 (2012).
- 356 14. Marcuse D. "Light Transmission Optics," (Van Nostrand Reinhold Company) (1972).
- 357 15. Martin B., Morand A., Benech P., Leblond G., Blaize S., Lerondel G., Royer P., Kern P. and Le Coarer E. "Design of
358 a new compact Static Fourier Transform Spectrometer in integrated optics based on a leaky loop structure," *Opt. Lett.*
359 **34** 184–186 (2009).
- 360 16. Pohl D., Escalé M. R., Madi M., Kaufmann F., Brotzer P., Sergejev A., Guldemann B., Giaccari P., Alberti E., Meier
361 U. and Grange R. "An integrated broadband spectrometer on thin-film lithium niobate," *Nat. Photonics* **14** 24–29
362 (2020).
- 363 17. Cheng Y., Sugioka K., Midorikawa K., Masuda M., Toyoda K., Kawachi M., Shihoyama K. "Control of the
364 cross-sectional shape of a hollow microchannel embedded in photostructurable glass by use of a femtosecond laser,"
365 *Opt. Lett.* **28** 55–57 (2003).
- 366 18. Osellame R., Taccheo S., Marangoni M., Ramponi R., Laporta P., Polli D., De Silvestri S., Cerullo G. "Femtosecond
367 writing of active optical waveguides with astigmatically shaped beams," *J. Opt. Soc. Am. B* **20** 1559–1567 (2003).
- 368 19. Welch P. "The use of fast Fourier transform for the estimation of power spectra: a method based on time averaging
369 over short, modified periodograms," *IEEE Transactions on audio electroacoustics* **15** 70–73 (1967).